Superconductivity in HfS_2 at ultrahigh pressure

Shihui Zhang,[1,2] Hailun Wang,[2] Hao Liu,[4] Jiapeng Zhen,[2] Shun Wan,[2] Wen Deng,[2]
Yonghao Han,[1] Bin Chen,[2,3,*] and Chunxiao Gao[1,†]

[1]*State Key Laboratory for Superhard Materials, Jilin University, Changchun 130012, China*
[2]*Center for High Pressure Science and Technology Advanced Research, Shanghai 201203, China*
[3]*School of Science, Harbin Institute of Technology, Shenzhen 518055, China*
[4]*School of Marine Technology and Environment, Dalian Ocean University, Dalian 116023, China*

(Received 6 May 2023; revised 5 August 2023; accepted 25 September 2023; published 31 October 2023; corrected 11 December 2023)

Adjusting the electrical and optical properties of two-dimensional materials by pressure is an important method to realize their applications in the fields of electronics and optoelectronic devices. Here, we report the highly tunable transport properties of the layered semiconductor HfS_2 under high pressure, including metallization and superconducting transition. HfS_2 is one of the IVB group transition-metal dichalcogenides, exhibiting a large band gap in ambient condition. The bandgap decreases from ∼2.0 to ∼1.1 eV within 15 GPa by pressure tuning, and HfS_2 becomes metallic at ∼60 GPa. Moreover, a superconducting transition is observed under ∼126 GPa, and the superconducting critical temperature (T_c) increases with further compression, reaching ∼4.4 K at ∼153 GPa. Hall-effect measurements show that pressure changes the carrier-concentration type from electron dominated to hole dominated at ∼145 GPa. Two structural transitions are found at moderate pressure, and one of them agrees with the changes observed in absorption and Raman spectroscopy measurements. Manipulation of the transport and optical properties of HfS_2 by pressure provides important information for its practical applications.

DOI: 10.1103/PhysRevMaterials.7.104802

I. INTRODUCTION

Transition-metal dichalcogenides (TMDs) [1] have attracted great interest in materials science and condensed-matter physics due to their novel physical properties and potential applications [2,3], especially in the fields of electronics and optoelectronics. Among them, transition-metal disulfides $MX_2 (X = S, Se, Te)$ are representative due to their abundant properties and versatility under compression [4]. Most of these materials have a hexagonal lattice structure similar to graphene, and the types of symmetry can be controlled by sample synthesis. Since interlayer interactions are sensitive to compression, pressure engineering becomes an efficient way to modulate the physical properties of MX_2 materials. Specifically, phenomena such as charge-density waves (CDW) [5–7], superconductivity [7–11], and Mott transitions [11] have been found in transition-metal disulfides through pressure modulation [12].

Different from 3*d* sulfides, 4*d* and 5*d* systems exhibit stronger spin-orbit coupling, higher levels of hybridization, and more diffuse orbitals [13]. Therefore, materials containing 4*d* and 5*d* centers generally have reinforcing or emergent properties [14–17]. Theoretical calculations show that the mobility in HfS_2 at room temperature is much higher than in MoS_2 [18]. The lamellar current density of HfS_2-based field-effect transistors is about 80 times higher than MoS_2 [19]. Few-layer HfS_2 field-effect transistors were fabricated by Kanazawa *et al.*, and high drain currents and mobility were observed [20]. As a clean tuning method, pressure can directly modify the lattice parameters and effectively change its electronic structures and optical properties. Previous studies found that HfS_2 is sensitive to strain and pressure. The band-gap state, gap energy, and phase transition of monolayer HfS_2 can be tuned by strain engineering in different deformation modes [21]. Calculations show that the thermoelectric properties of monolayer HfS_2 can be significantly improved by introducing stress [22]. Recently, studies have shown that the Raman peaks of bulk HfS_2 have abnormal changes at 5.7–9.8 and 12.8-15.2 GPa [23], and structural transitions and metallization in HfS_2 under pressure have been reported [24]. However, the minimum temperature measured by the variable-temperature electrical conductivity measurements in these results is only 120 K, and the evidence of structural transformation is insufficient. Therefore, further high-pressure studies with solid evidence of metallization and potential superconducting transition are needed to fully understand the high-pressure behavior of HfS_2.

Here, we have investigated HfS_2 by electrical transport measurements, optical absorption, Raman spectroscopy, and synchrotron x-ray diffraction (XRD) measurements. Metallization was confirmed to occur above 50 GPa and superconductivity was observed at ∼126 GPa, with the T_c increasing with pressure (∼4.4 K at 153 GPa). Hall coefficients show a change in carrier-concentration type from electrons to holes at about 145 GPa, implying a change in electronic structure. Optical absorption reveals the evolution of the band gap. A highly tunable band gap of HfS_2 under pressure is found, which decreases from ∼2.0 to ∼1.1 eV within 15 GPa. XRD and spectroscopic results show that there are two

*Corresponding author: chenbin@hpstar.ac.cn
†Corresponding author: cc060109@qq.com

 ©2023 American Physical Society

structural phase transitions at around 11 and 35.5 GPa. Finally, a possible phase diagram of HfS_2 as a function of pressure and temperature is summarized.

II. EXPERIMENTS

HfS_2 single crystals were purchased from HQ-graphene. The sample was characterized by XRD combined with energy-dispersive spectroscopy. Two runs (run 1 and run 2) of electrical transport measurements (van der Paul method) were conducted. Diamond-anvil cell was used to create pressure, with a nonmagnetic copper-beryllium alloy disk between the anvils as gasket. An insulating layer of cubic boron nitride (cBN) was prepared on the prepressed gasket. The diameters of the anvil culets in run 1 and run 2 were 100 and 200 μm, respectively. The sample was loaded into the chamber directly without a pressure-transmitting medium (PTM). Platinum foils were used as electrodes that contacted the sample in the chamber. The temperature-dependent resistance was measured with Quantum Design's PPMS (2-300 K, 0-9 T).

As for optical and spectroscopy measurements, the high-pressure experiments were performed with a DAC with 300−μm-culet diamonds, and T301 steel gaskets were used. Silicone oil was loaded as the PTM. *In situ* high-pressure ultraviolet-visible near-infrared (UV-VIS-NIR) absorption spectra were measured on a custom spectroscopy system (Gora-UVN-FL, Ideaoptics, Shanghai, China). And, a 633-nm laser-excited micro-Raman system (Renishaw, UK) was used to obtain Raman spectra of the sample.

III. RESULTS AND DISCUSSION

The temperature-dependent resistance $R(T)$ of HfS_2 for two runs from ∼7.6 to ∼153 GPa is shown in Fig. 1. Figure 1(a) is the results of run 1, where the $R-T$ curve exhibits a typical semiconductor behavior under low pressure ($P <\sim 60$ GPa). Around 60.6 GPa, the $R-T$ curves in the high-temperature range exhibit metallic behavior, while there is still the semimetallic trend below ∼175 K. With the pressure increasing, the rising trend of the low-temperature resistance is further suppressed, suggesting the completion of the semiconductor-to-metal transition. Figures 1(b)–1(f) are the results of the second run, and it can be seen that the $R-T$ curve shows metallic across the entire temperature range when the pressure is increased to 65 GPa. Importantly, the superconducting transition, characterized by a sharp decrease in $R(T)$, starts to appear at pressure above 126 GPa, as shown in Fig. 1(b). The critical temperature of the superconducting transition T_c defined as the temperature at which the resistance drops to 90% is enhanced from 2 K at 126 GPa to 4.4 K at 153 GPa. By analyzing the normalized resistance at 10 K in Fig. 1(c), it is found that the resistance drop is almost ∼80% of the normal state value within the temperature from 4.4 to 2.0 K under 153 GPa. Due to the nonhydrostatic pressure condition, the large pressure gradient across the sample may broaden the transition temperature range and produce a nonzero resistance in the superconducting state [9,25]. Notably, the T_c of HfS_2 monotonically increases from 126 to 153 GPa and there is a high possibility that higher T_c can be obtained by higher pressure.

To further confirm the presence of pressure-induced superconductivity in HfS_2, resistance measurements were performed under an external magnetic field. Figure 1(e) shows the $R-T$ curves at 153 GPa under different magnetic fields applied along the crystal c axis from 0 to 1.4 T. It can be seen that as the magnetic field increases; T_c is clearly suppressed to lower temperatures, which is typical in the bulk superconducting transition. Figure 1(f) displays the upper critical field $\mu_0 H_{C2}$ as a function of critical temperature T_c. $\mu_0 H_{C2}(T_C)$ was fitted by the single-band Werthamer-Helfand Hohenberg (WHH) formula and the Ginzburg-Landau (GL) equation, respectively. The upward curvature of $\mu_0 H_{C2}(T_C)$ near the zero-field limit is inconsistent with the WHH theory. A well-fitted curve of $H_{C2}(T)$ can be obtained by using the empirical formula $\eta_{c2}(T) = \eta_{c2}(-T/T_c)^{1+\alpha}$ [26,27]. Similar positive curvature of $\eta_{c2}(T)$ was first discovered in UPt_3 and URu_2Si_2, and it has been attributed to the coexistence of charge-density wave, multiband effect, strong coupling, and field- and temperature dependence of normal state parameters [28,29].The positive curvature is also found in TaS_2 and $TaSe_2$, which have similar structures to HfS_2. Considering the previously discovered two-band model in NbS_2 [30] and $NbSe_2$ [31], the fit suggests that instead of the WHH single-band model, a multiband superconducting pair state is likely to exist in the sample. The fitted upper critical field $H_{c2}(0)$ at 0 K is 2.37 T (WHH) and 4.37 T (GL), respectively. $H_{c2}(0)$ is much smaller than the Bardeen-Cooper-Schrieffer weakly coupled Pauli paramagnetic limit [32,33], $\mu_0 H_p = 1.84\ T_c = 8.1$ T for $T_c = 4.4$ K. The validity of the Pauli limit field implies the existence of phonon-mediated superconductivity in HfS_2 [9].

The Hall effect of materials reflects the conduction mechanism, energy band structure, etc. And, the Hall coefficient R_H is an important parameter for studying and understanding the electronic structure evolution of superconductivity under pressure. The Hall measurement was performed on HfS_2 at the temperature of 10 K, the current is applied in the *a-b* plane, and the magnetic field is in the direction perpendicular to the *a-b* plane. The dependence of R_H on pressure is shown in Fig. 2(b). It can be seen that R_H is always negative from 60 to 133 GPa. Thus, the dominant charge carriers are electronics (n type). As the pressure reaches 145 GPa, R_H increases and turns to positive, and the dominant carriers change from electrons to holes (p type). The transformation of carrier type indicates that the energy band structure near the Fermi surface of HfS_2 changes during the compression process and the orbit across the Fermi surface changes. Carrier concentration as a function of pressure can be calculated through R_H, as shown in Fig. 2(a). After metallization, starting from 60 GPa, the effective carrier concentration increases linearly with pressure until the superconducting transition occurs at 126 GPa. When the R_H turns to positive, the corresponding carrier concentration tends to show an upward trend, starting from 130 GPa. Correspondingly, the T_c increases faster from this point. The emergence of superconducting transition and the larger increasing rate of T_c is accompanied by a steady increase in carrier concentration and a change in carrier type. Therefore, the important factor determining the change of T_c could be the pressure-induced redistribution of the energy-state density near the Fermi surface of HfS_2. In fact, this correlation between pressure-induced Fermi-surface anomalies

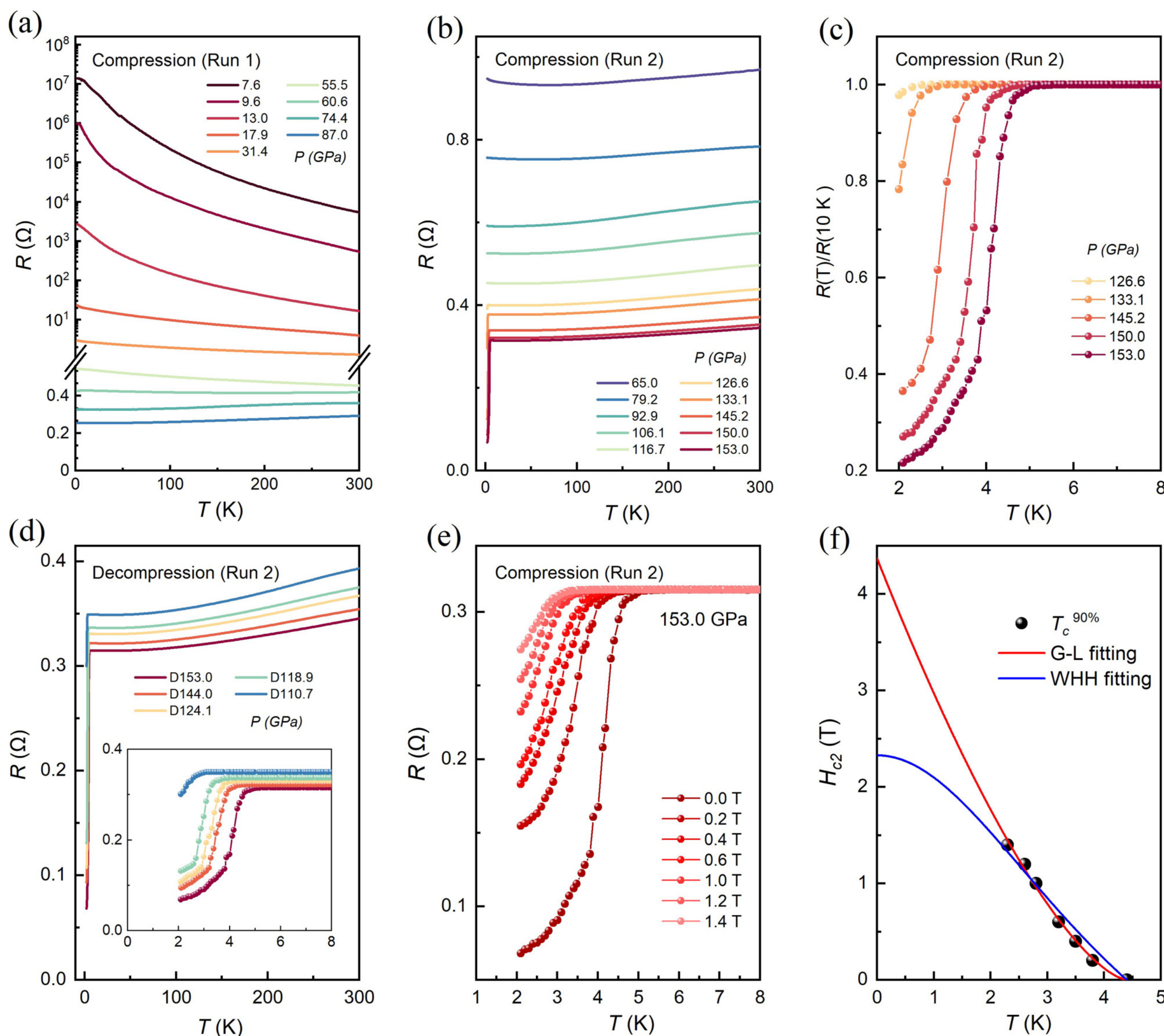

FIG. 1. Temperature dependence of the resistance of HfS_2 samples at different pressures: (a) Compression process in run 1; (b) compression process in run 2; and (c) temperature-dependent normalized resistance in run 2 at 10 K, which shows nearly 80% decrease in resistance at 153 GPa. (d) Decompression process in run 2; (e), (f) determination of zero-temperature upper critical magnetic field $\mu_0 H_{C2}(0)$ of HfS_2 at $\sim$ 153 GPa. (e) $R-T$ curve under external magnetic field up to 1.4 T with step of 0.2 T. (f) $\mu_0 H_{C2}$-T phase diagram. Solid line in blue and red represents fitting by WHH formula and GL equation, respectively.

and superconductivity are the key to initial the discovery of the CDW state and its competition with superconductivity, and it also provides an important reference for our conjecture [34,35].

In order to investigate the effect of pressure on the optical and electronic properties of HfS_2, optical UV-VIS-NIR absorption measurements were carried out, as shown in Fig. 3. A series of images of samples under different pressures are shown in Fig. 3(a). The initial sample is transparent and in tangerine. The color of the sample darkens as the pressure increases, turning to brown at 11.6 GPa, and becomes blackish when the pressure increase to 17.1 GPa. UV-VIS-NIR absorption spectra provide more information. At 0.2 GPa the emergence of an absorption edge corresponding to an indirect optical band gap of $\sim$1.96 eV is observed and is in good agreement with previous results [36]. When pressure increases, the absorption edge moves to a lower-energy region, as shown in Fig. 3(b). The evolution of the band gap as a function of pressure is obtained by fitting the Tauc equation $(\alpha h\nu)^{0.5} = \alpha(h\nu - E_g)$, as shown in Fig. 3(c). Since the absorption spectrum data at 17.1 GPa exceed the range of the measurement instrument and is improper to be fitted by the Tauc equation, Fig. 3(c) only shows the transformation of the optical band gap up to 15.6 GPa. Below $\sim$11 GPa, the band gap of HfS_2 decreases linearly with the increased pressure, and it decreases more rapidly at higher pressures. The abrupt change is shown in the slope of the pressure–band-gap curve.

In order to obtain the vibration characteristics of the sample and study the structure change of HfS_2 under high

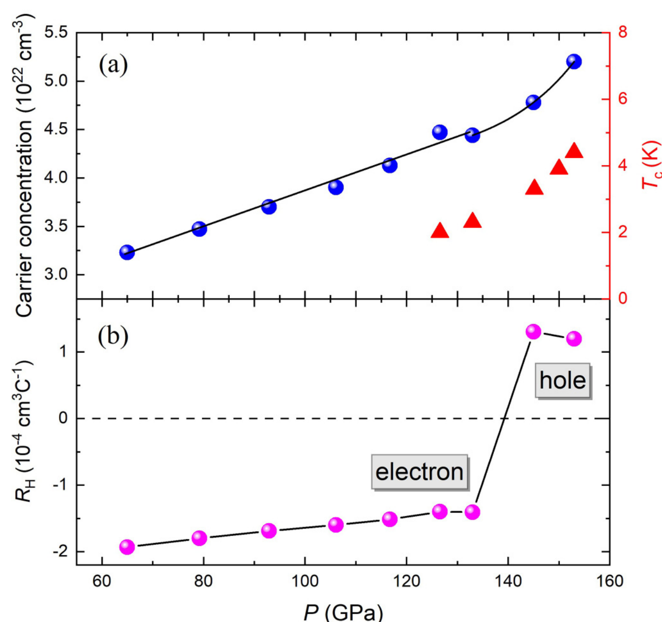

FIG. 2. Hall-effect measurements at 10 K under high pressure. (a) Carrier concentration of HfS_2 under compression in run 2. Vertical coordinate on right side is T_c at different pressures. There is high correlation between carrier concentration and T_c. (b) Pressure-dependent Hall coefficient (R_H) at 10 K.

pressure, *in situ* Raman spectra up to 50 GPa were measured. As shown in Figs. 4(a)–4(d), HfS_2 has six normal vibrational modes: $\Gamma = A_{1g} + E_g + 2A_{2u} + 2E_u$. The A_{1g} and E_g modes are Raman-active modes and the A_{2u}(LO), A_{2u}(TO), E_u(LO), and E_u(TO) are infrared-active modes [37–39]. The Raman spectrum of HfS_2 measured at 0.7 GPa consists of four modes [see Fig. 4(a)] with frequencies at ≈138, 262, 323, and 342 cm^{-1}, respectively. This is consistent with prior research [23,38,39] and demonstrates the high purity of the single-crystal sample. The peaks at 262 and 342 cm^{-1} were attributed to E_g modes, corresponding to the the in-plane vibrational mode of the S–Hf–S lattice and A_{1g} mode is corresponding to the out-of-plane vibrational mode, respectively. The peak at 325 cm^{-1} is attributed to an IR-active E_u(LO) [13,39] or A_{2u}(LO) [24,38] similar mode. Due to the long-range Coulomb forces resulting from charges localized on atoms, both the LO and TO components of infrared-active modes can be observed in the Raman spectrum despite the formal Raman inactivity [38]. Previously, resonance properties of Raman spectrum involving such phonons have been reported [36]. This paper will be attributed to A_{2u}(LO). The weak feature at 138 cm^{-1} is assigned to E_u(TO) [13].

As the pressure increases, all vibration modes move toward higher wave numbers [see Fig. 4(b)]. The pressure coefficient of A_{1g} mode is significantly higher than that of E_g mode, which indicates that the effect of pressure on the external vibration is more pronounced than that on the internal vibration. When the pressure increases to about 11.3-14.8 GPa, the $M3$ vibrating mode disappears, and a new Raman peak $M4$ appears at about 339 cm^{-1}. The pressure coefficients of E_g, A_{1g}, and $M1$ modes show a significant discontinuity, indicating a typical structural transition. As the pressure continues to increase above 14.8 GPa, $M1$, E_g, $M4$, and A_{1g} continue to blueshift and gradually weaken until all Raman peaks disappear under about 50 GPa, corresponding to the metallization behavior under about 60 GPa in the electrical transport experiments.

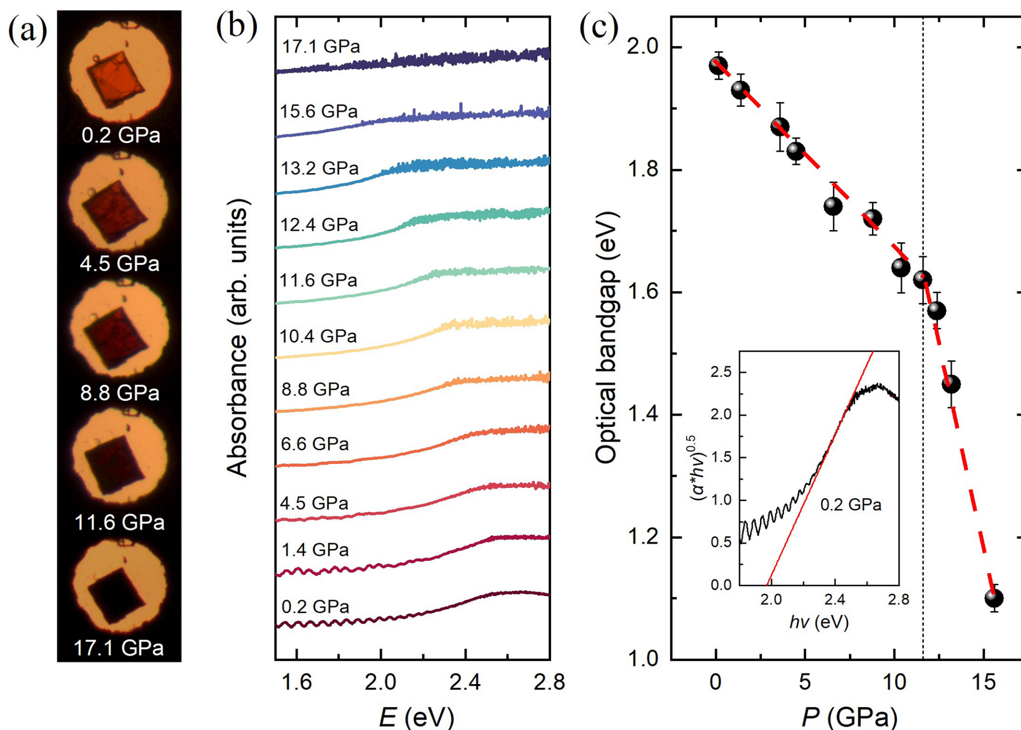

FIG. 3. Results of absorption spectra of HfS_2 under high pressure. (a) Optical images of sample under different pressure in DAC chamber. (b) Representative optical absorption spectra of HfS_2 under high pressure. (c) optical bandgap as a function of pressure.

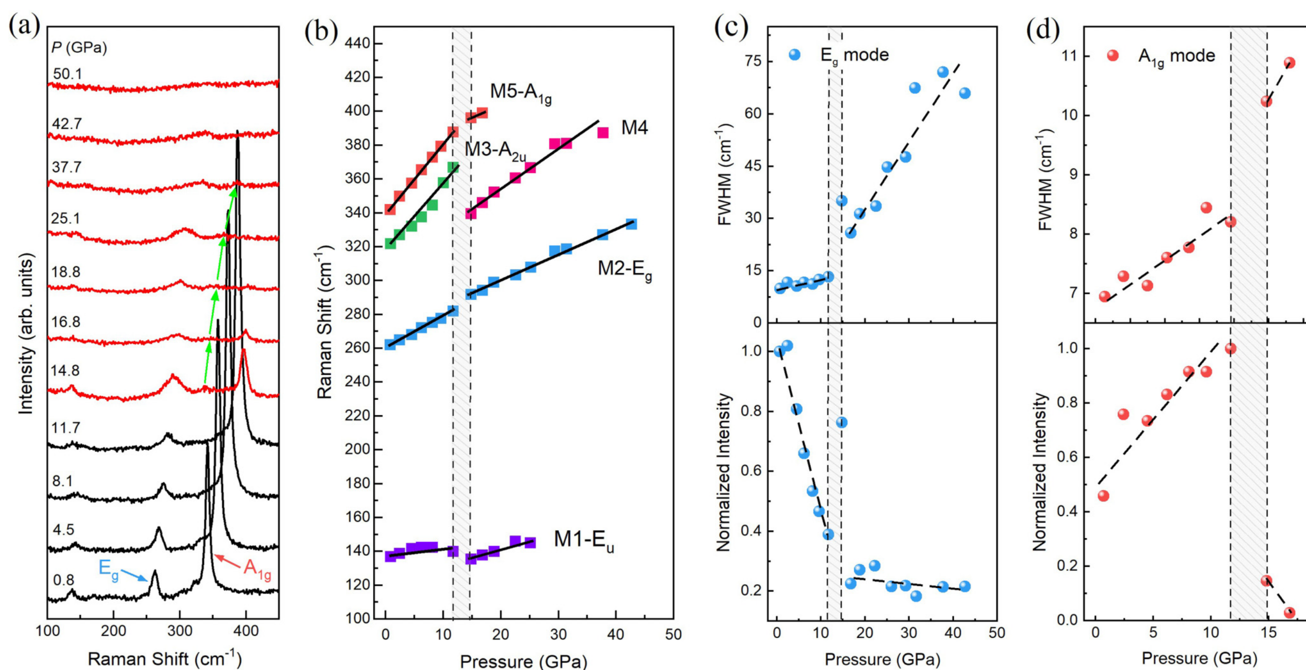

FIG. 4. (a) Raman spectra of HfS_2 at room temperature from ambient pressure to 50.1 GPa. (b) Evolution of each vibrational mode during compression. (c), (d) FWHM and normalized intensity of A_{1g} and E_g modes.

In order to further confirm and analyze the abnormal changes of Raman vibration, we analyzed the full width at half maximum (FWHM) and normalized intensity of E_g and A_{1g}, as shown in Figs. 4(c) and 4(d). For the E_g mode between 0 and ∼11.3 GPa, the FWHM slowly increases with pressure, while the intensity decreases rapidly. When the pressure rises to 14.8 GPa, the Raman peak broadens rapidly, while the intensity decreases slowly after the transition. For the A_{1g} mode in the range of 0-11.3 GPa, the FWHM increases slowly, and the intensity continues to increase. The FWHM increases rapidly after the pressure reaches 14.8 GPa, and the intensity suddenly decreases by about 80%.

To confirm the structural properties of HfS_2 under high pressure, we collected the XRD results up to ∼125 GPa [see Fig. S3(a)]. Two structural transitions were found at ∼11.0 and ∼35.5 GPa, which were referred to as phase I and phase II, respectively. After the pristine phase $P-3m1$ was compressed to 11.0 GPa, three peaks appeared, indicating the beginning of a structural transformation. Further compressing of the sample to 15.5 GPa revealed the increasing of the intensity of these peaks, while the peaks from the original structure weakened, and some peaks even disappeared. When the pressure was increased to 35.5 GPa, another two peaks appeared, and the transition to phase II occurred. In the subsequent compression up to 125 GPa, no new diffraction peaks could be observed. It is noteworthy that when the pressure is increased above 13.8 GPa, the peak intensity weakens and the structure starts to be disordered, as shown by the appearance of broad peaks, indicating the possibility of an amorphous phase in addition to the crystalline phase [40,41]. We calculated the enthalpy of $P-3m1$ and other potential structures in the range of 0-125 GPa. As shown in Fig. S3(b), the *Pnma* phase has a lower enthalpy compared with the $P-3m1$ phase when the sample is compressed to ∼10.0 GPa [42]. When the pressure is above 30.0 GPa, the $I4/mmm$ phase is energetically more favorable than the *Pnma* phase. Therefore, our experimental and theoretical calculation results show that there are two structural transitions in HfS2: at about 11.0 GPa, there is a transition from $P-3m1$ phase to *Pnma* phase, and at 35.5 GPa, there is a structural transition from *Pnma* phase to $I4/mmm$ phase. The first structural transition is in good agreement with the anomalous pressure changes observed in the UV absorption and Raman-scattering results.

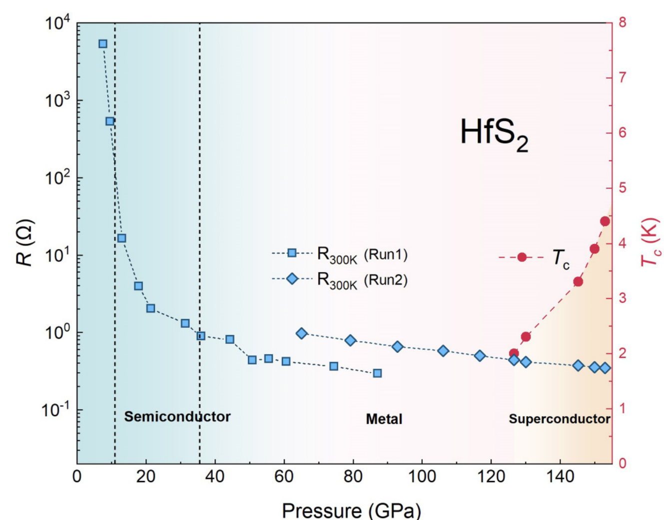

FIG. 5. Schematic pressure-temperature (P-T) phase diagram of HfS_2. Blue and pink regions demarcate semiconducting and metallic states, respectively. Yellow region corresponds to superconducting states. Black dotted line indicates pressure of structural phase transition.

Figure 5 schematically illustrates the whole picture of this research. Electrical transport measurements, along with XRD and spectroscopy measurements, reveal a significant correlation between electronic, vibrational, and structural transitions in HfS_2 at 11 GPa. Metallization occurs after a structural transition at 35.5 GPa. We believe that the metallization in HfS_2 is closely related to the change of the electronic structure caused by the pressure-induced reduction of the interlayer distance. With further compression, the sample remained in phase II without further structural transformation. The detected superconductivity after metallization has nothing to do with the structural phase transition, but corresponds to the steady increase of carrier-concentration and carrier-type changes under high pressure. That is to say, the change of the electronic band structure near the Fermi surface is the key to understanding the transport behavior of HfS_2 at high pressures.

IV. CONCLUSION

In summary, the structural, electrical, vibrational, and optical properties of HfS_2 under high pressure are reported. It is found that HfS_2 transforms into a superconductor above 126 GPa, and T_c reaches ~4.4 K at 153 GPa with increasing compression. The Hall-effect measurement detects a change in carrier type and the increase in carrier concentration, which corresponds with the upward trend of T_c at very high pressures. In addition, two structural phase transitions were observed. The structural transition at ~11 GPa explains the abnormal changes of the optical band gap and Raman vibration mode in the low-pressure range. Our study not only reveals pressure-induced superconductivity in HfS_2, but also enriches the understanding of the structural changes and electronic states of TMDs. A highly tunable band gap of HfS_2 under pressure was also discovered, which can be tuned from ~2.0 to ~1.1 eV within 15 GPa. This provides a window for more applications of HfS_2 in optoelectronic devices, such as high-performance field-effect transistor, photovoltaic cells, and infrared optoelectronic devices.

ACKNOWLEDGMENTS

This work was supported by the National Natural Science Foundation of China (Grants No. U1530402 and No. 12274101). We are grateful to the beamline station BL15U1 of the Shanghai Synchrotron Radiation Facility (SSRF) for experimental support of high-pressure synchrotron XRD. We are grateful to Mingzhi Yuan (HPSTAR) for helping in revising the manuscript.

[1] Y. I. Joe, X. Chen, P. Ghaemi, K. Finkelstein, G. de La Peña, Y. Gan, J. Lee, S. Yuan, J. Geck, and G. MacDougall, Nat. Phys. **10**, 421 (2014).

[2] M. N. Ali, J. Xiong, S. Flynn, J. Tao, Q. D. Gibson, L. M. Schoop, T. Liang, N. Haldolaarachchige, M. Hirschberger, and N. P. Ong, Nature (London) **514**, 205 (2014).

[3] I. Pletikosić, M. N. Ali, A. V. Fedorov, R. J. Cava, and T. Valla, Phys. Rev. Lett. **113**, 216601 (2014).

[4] S. Manzeli, D. Ovchinnikov, D. Pasquier, O. V. Yazyev, and A. Kis, Nat. Rev. Mater. **2**, 1 (2017).

[5] D. C. Freitas, P. Rodière, M. R. Osorio, E. Navarro-Moratalla, N. M. Nemes, V. G. Tissen, L. Cario, E. Coronado, M. García-Hernández, and S. Vieira, Phys. Rev. B **93**, 184512 (2016).

[6] M. Leroux, I. Errea, M. Le Tacon, S.-M. Souliou, G. Garbarino, L. Cario, A. Bosak, F. Mauri, M. Calandra, and P. Rodiere, Phys. Rev. B **92**, 140303(R) (2015).

[7] B. Wang, Y. Liu, X. Luo, K. Ishigaki, K. Matsubayashi, W. Lu, Y. Sun, J. Cheng, and Y. Uwatoko, Phys. Rev. B **97**, 220504(R) (2018).

[8] Q. Dong, J. Pan, S. Li, Y. Fang, T. Lin, S. Liu, B. Liu, Q. Li, F. Huang, and B. Liu, Adv. Mater. **34**, 2103168 (2022).

[9] Z. Chi, X. Chen, F. Yen, F. Peng, Y. Zhou, J. Zhu, Y. Zhang, X. Liu, C. Lin, S. Chu *et al.*, Phys. Rev. Lett. **120**, 037002 (2018).

[10] Z.-H. Chi, X.-M. Zhao, H. Zhang, A. F. Goncharov, S. S. Lobanov, T. Kagayama, M. Sakata, and X.-J. Chen, Phys. Rev. Lett. **113**, 036802 (2014).

[11] B. Sipos, A. F. Kusmartseva, A. Akrap, H. Berger, L. Forró, and E. Tutiš, Nat. Mater. **7**, 960 (2008).

[12] A. H. Castro Neto, Phys. Rev. Lett. **86**, 4382 (2001).

[13] S. N. Neal, S. Li, T. Birol, and J. L. Musfeldt, npj 2D Mater. Appl. **5**, 45 (2021).

[14] Y. Ma, L. Kou, B. Huang, Y. Dai, and T. Heine, Phys. Rev. B **98**, 085420 (2018).

[15] G. Cao, J. Terzic, H. D. Zhao, H. Zheng, L. E. De Long, and P. S. Riseborough, Phys. Rev. Lett. **120**, 017201 (2018).

[16] T. Birol and K. Haule, Phys. Rev. Lett. **114**, 096403 (2015).

[17] S. S. Cheema, D. Kwon, N. Shanker, R. Dos Reis, S.-L. Hsu, J. Xiao, H. Zhang, R. Wagner, A. Datar, and M. R. McCarter, Nature (London) **580**, 478 (2020).

[18] W. Zhang, Z. Huang, W. Zhang, and Y. Li, Nano Res. **7**, 1731 (2014).

[19] G. Fiori, F. Bonaccorso, G. Iannaccone, T. Palacios, D. Neumaier, A. Seabaugh, S. K. Banerjee, and L. Colombo, Nat. Nanotechnol. **9**, 768 (2014).

[20] T. Kanazawa, T. Amemiya, A. Ishikawa, V. Upadhyaya, K. Tsuruta, T. Tanaka, and Y. Miyamoto, Sci. Rep. **6**, 22277 (2016).

[21] M. Faghihnasiri, A. Ahmadi, S. Alvankar Golpayegan, S. Garosi Sharifabadi, and A. Ramazani, Nanomaterials **10**, 446 (2020).

[22] H. Wang, Y.-S. Lan, B. Dai, X.-W. Zhang, Z.-G. Wang, and N.-N. Ge, ACS Omega **6**, 29820 (2021).

[23] M. Grzeszczyk, J. Gawraczyński, T. Woźniak, J. Ibáñez, Z. Muhammad, W. Zhao, M. Molas, and A. Babiński, Acta Phys. Pol. A **141**, 95 (2022).

[24] M. Hong, L. Dai, H. Hu, X. Zhang, C. Li, and Y. He, J. Mater. Chem. C **10**, 10541 (2022).

[25] P. Wang, D. He, C. Xu, X. Ren, L. Lei, S. Wang, F. Peng, X. Yan, D. Liu, and Q. Wang, J. Appl. Phys. **115**, 043507 (2014).

[26] Q. Dong, Q. Li, S. Li, X. Shi, S. Niu, S. Liu, R. Liu, B. Liu, X. Luo, and J. Si, npj Quantum Mater. **6**, 20 (2021).

[27] T. Lin, X. Wang, X. Chen, X. Liu, X. Luo, X. Li, X. Jing, Q. Dong, B. Liu, and H. Liu, Inorg. Chem. **60**, 11385 (2021).
[28] L. DeLong, G. W. Crabtree, L. N. Hall, D. G. Hinks, W. K. Kwok, and S. K. Malik, Phys. Rev. B **36**, 7155 (1987).
[29] W. K. Kwok, L. E. DeLong, G. W. Crabtree, D. G. Hinks, and R. Joynt, Phys. Rev. B **41**, 11649 (1990).
[30] H. Suderow, V. G. Tissen, J. P. Brison, J. L. Martínez, and S. Vieira, Phys. Rev. Lett. **95**, 117006 (2005).
[31] V. G. Tissen, M. R. Osorio, J. P. Brison, N. M. Nemes, M. García-Hernández, L. Cario, P. Rodière, S. Vieira, and H. Suderow, Phys. Rev. B **87**, 134502 (2013).
[32] A. M. Clogston, Phys. Rev. Lett. **9**, 266 (1962).
[33] B. Chandrasekhar, Appl. Phys. Lett. **1**, 7 (1962).
[34] T. Smith, L. Delong, A. Moodenbough, T. Geballe, and R. Schwall, J. Phys. C: Solid State Phys. **5**, L230 (1972).
[35] S. Hillenius, L. Delong, and R. Coleman, Physica B+ C **105**, 123 (1981).
[36] K. Terashima and I. Imai, Solid State Commun. **63**, 315 (1987).
[37] T. Iwasaki, N. Kuroda, and Y. Nishina, J. Phys. Soc. Jpn. **51**, 2233 (1982).
[38] L. Roubi and C. Carlone, Phys. Rev. B **37**, 6808 (1988).
[39] A. Cingolani, M. Lugara, G. Scamarcio, and F. Lévy, Solid State Commun. **62**, 121 (1987).
[40] R. A. Susilo, Y. Liu, H. Sheng, H. Dong, R. Sereika, B. Kim, Z. Hu, S. Li, M. Yuan, and C. Petrovic, J. Mater. Chem. C **10**, 1825 (2022).
[41] Y. Xi, X. Jing, Z. Xu, N. Liu, Y. Liu, M.-L. Lin, M. Yang, Y. Sun, J. Zhuang, and X. Xu, J. Am. Chem. Soc. **144**, 18887 (2022).
[42] See Supplemental Material at http://link.aps.org/supplemental/10.1103/PhysRevMaterials.7.104802 for the experiment details, including sample characterization and high-pressure experimental details; the figure of pressure-dependence curve of Hall resistance under various pressures; structure evolution of HfS_2 sample at high pressure, including the synchrotron XRD patterns and the calculated enthalpy.

Correction: The “Corresponding author” identifiers and email addresses were missing at publication and have now been inserted.